Supporting Information

Zero-Wastewater-Discharge Noncontact Solar Desalter for Saline-Alkali Soil Remediation and Grain Yield Increase by Brackish Water

Xiangyang Dong[a], Xiangyu Luo[b], Zhenghui Huang[a], Shuai Ye[c], Chang Chen[d], Jingtao Xu[e], Zhen Wang[d], Xiaoliang Meng[c], Wensheng Zhao[b], Ronggui Yang[f], Chaoji Chen[a,], Hongbing Deng[a,]**

[a] Hubei Key Laboratory of Biomass Resource Chemistry and Environmental Biotechnology, Hubei International Scientific and Technological Cooperation Base of Sustainable Resource and Energy, Hubei Engineering Center of Natural Polymers-based Medical Materials, School of Resource and Environmental Science, Wuhan University, Wuhan 430079, China

[b] Key Laboratory of Hydraulic Machinery Transients, Ministry of Education, Wuhan University, Wuhan 430072, China

[c] School of Remote Sensing and Information Engineering, Wuhan University, Wuhan, 430079, China

[d] State Environmental Protection Key Laboratory of Soil Health and Green Remediation, College of Resource and Environment, Huazhong Agricultural University, Wuhan 430070, China

[e] School of Materials and Chemical Engineering, Ningbo University of Technology, Ningbo 315016, China

[f] State Key Laboratory of Coal Combustion, School of Energy and Power Engineering, Huazhong University of Science and Technology, Wuhan, Hubei, 430074 P. R. China

[*]E-mail: chenchaojili@whu.edu.cn (C. C.); hbdeng@whu.edu.cn (H. D.)

Supplementary Material includes:

Supplementary Notes 1-8;

Supplementary Figures 1-29;

Supplementary Tables 1-6.

Supplementary Movies 1-3

Supplementary Notes

Supplementary Note 1

The mechanism of environmental energy enhancement has been explained by Liu et al., but in this design, it is slightly different due to the noncontact photothermal conversion and utilization mode. The heat transfer process includes three energy flows: solar energy input, steam output, and heat exchange with the environment. The solar energy input includes direct solar energy input and infrared light input converted through mulching film.

The energy transfer process can be expressed as the following equations:

$$mH_v = Q_s + Q_t \#(1)$$

$$Q_T = P_s S_t A_t - S_t h_t (T_t - T_e) - \varepsilon\sigma S_t \left(T_t^4 - T_e^4\right) \#(2)$$

$$Q_s = V A_s S_s P_m - S_{s\cdot eff} h_s (T_s - T_e) - \varepsilon\sigma S_s \left(T_s^4 - T_e^4\right) - k S_b (T_s - T_w) \#(3)$$

in which, m is the mass of evaporated water, H_v is the enthalpy of phase change, Q_s is the energy exchange between the side of the desalter and the external, including absorption of infrared radiation from mulching film and , Q_t is the energy exchange between the top of the desalter and the external, P_s is the solar power, S_t and S_s are the top and side area of the desalter, A_t is the sunlight absorptivity of the top of the desalter, h_t and h_s are the convective heat transfer coefficients at the top and side of the desalter, T_t and T_s are the temperature at the top and side of the desalter, and T_e is the ambient temperature, ε is the emissivity, σ is the Stefan-Boltzmann constant, A_s is the infrared light absorptivity of the wet paper, P_m is the infrared emission power of the mulching film, Ss.eff is the effective area of side surface for convective heat transfer, k is the thermal conductivity of the desalter, S_b is the bottom area of the desalter in contact with water, and T_w is the temperature of the bulk water at the bottom. Due to the fact that the infrared light emitted by the mulching film does not shine vertically on the side of the desalter, there is a factor V used to correct this geometric influence.

When the paper is wetted, due to the irregular movement of water molecules on the surface of the paper, collisions occur between water molecules, causing some water molecules to have a decrease in energy and others to have an increase in energy. Part of the high-energy water molecules have the opportunity to break free from the attraction of the liquid and enter the air to form vapor, forming a saturated water vapor boundary layer near the liquid surface that is isothermal with the liquid (Figure S9). Due to the departure of high-energy water molecules, the average kinetic energy of the water molecules decreases, which is manifested macroscopically as a decrease in temperature. If the vapor partial pressure in the boundary layer is greater than the ambient vapor partial pressure, water molecules in the boundary layer will diffuse toward the surrounding environment. At the same time, water molecules in the liquid

will also diffuse into the boundary layer, keeping the boundary layer continuously saturated. The migration path of water molecules from the liquid to the boundary layer, then to the surrounding environment ultimately forms, which manifested macroscopically as continuous evaporation of water and continuous decrease in liquid temperature. Due to the continuous decrease in liquid temperature, the temperature of the boundary layer will also decrease synchronously, and the vapor partial pressure of the boundary layer will also decrease, ultimately equal to the ambient vapor partial pressure. The liquid temperature ultimately stabilizes at the wet bulb temperature of the ambient air. It can be found that the lower the air humidity, the greater the decrease in liquid temperature on the surface of the paper.

In our design, the desalter is composed of paper wrapped around the straw, and its top interface is circular with a very small area, so the energy exchange Q_t with the external can be almost negligible. Due to the fact that the side temperature of our desalter can always remain below the ambient temperature, an energy gain (Q_s>0) from the environment is achieved, which will promote the vapor generation process.

Supplementary Note 2

The wicking process in water was divided into two stages. The first hour was a rapid upward phase. The wicking height gradually increased with time. The climbing speed was the fastest and reached a height of 11.86 cm. After 1 h there was a stable stage that had a slow climbing speed. The wicking height increased only by 1.98 cm from the 60^{th} min to the 120^{th} min. Considering the length of the part inserted into soil or water, we selected 23 cm as the length of the desalter.

Although the mass change of the desalination device seemed proportional to time, it could still be divided into two stages, similar to the wicking process, namely an acceleration stage of mass loss within 1 h and a stable stage after 1 h. The existence of the two stages was confirmed by the variation in evaporation rate with time (Figures 2e and f). The reason for the two-stage variation of mass change and evaporation rate was that they were closely related to wicking height. The higher the wicking height, the larger the side area of the desalter for evaporation, and the mass change and evaporation rate were also more prominent. Therefore, mass changes and evaporation rate were highly synchronized with wicking height. During interfacial evaporation, the salt gradually crystallized on the surface of the column desalter, forming a rough surface (Figure S10). Interestingly, the crystallization of brine with different salt concentrations exhibited positional selectivity on the surface of the desalter (Figure S11). This selectivity occurred because the brine continuously evaporated and concentrated while being

wicked towards the top of the desalter, and high-concentration brine reached saturation first and crystalized at the bottom of the desalter, while low-concentration brine reached saturation late, thus crystallizing at the top of the desalter.

The evaporation rate of the desalter was not affected by salinity in low-concentration salt water, and even slightly increased (Figure S12). First, this was because of the noncontact photothermal conversion and utilization mode. The mulching film for photothermal conversion did not contact the brine, and there was no salt crystallization on the surface; thus, unlike traditional desalination devices, our desalination device would not be troubled by a decreased evaporation efficiency caused by the accumulated salt on the surface of the photothermal material. Second, the salt crystallized on the surface of the paper-based desalter expanded the evaporation area, which raised the evaporation rate. Notably, the salt crystals on the surface of the desalter could be removed easily and collected by gentle tapping (Movie S1 and Figure S13), which made the regeneration of the desalter extremely facile and opened a new path for collecting and using the salt.

A 10×10 array was manufactured to study the evaporation rate of an expanded desalter array under natural light (Figure S14). Although the light power density was less than 0.5 kW m^{-2}, the average evaporation rate still reached 24.12 kg m^{-2} h^{-1}; thus, the expanded desalter array still maintained a high evaporation rate and adapted well to dull natural light. The prototype of an expanded desalter array with a condensing shell further confirmed the potential for large-scale application of this columnar desalter. Huanghai Sea seawater was added to the desalination device. When it was exposed to sunlight, water with an ion concentration three orders of magnitude lower than seawater quickly condensed on the surface of the shell (Figures S15 and S16), and this condensed freshwater could be used for drinking or saline-alkali soil remediation.

Supplementary Note 3

The water in the soil remediation system came mainly from irrigation water and soil water storage. Soil and irrigation water were also the primary sources of salt in this system. When freshwater, brackish water, seawater, or brine was irrigated into the soil, the salt in the soil dissolved in these waters, forming saliferous soil extract. The salinity of soil extract ($c_{soil\ extract}$) was shown by the following formula:

$$c_{soil\ extract} = \frac{m_{soil}\, c_{initial\ soil} + m_{irrigation\ water}\, c_{irrigation\ water}}{m_{irrigation\ water} + m_{soil}\, c_{initial\ soil} + m_{irrigation\ water}\, c_{irrigation\ water}} \#(4)$$

Here, $c_{soil\ extract}$ was the salinity of soil extract. m_{soil} was the mass of soil. $c_{initial\ soil}$ was the salinity of soil without remediation. $m_{irrigation\ water}$ was the mass of irrigation water. $c_{irrigation\ water}$ was the salinity of irrigation water. $c_{soil\ extract}$ was the salinity of soil extract.

Because $c_{initial\ soil}$ and $c_{irrigation\ water}$ were usually less than 1% and 2%, $m_{soil}\ c_{initial\ soil}$ and $m_{irrigation\ water}\ c_{irrigation\ water}$ were much smaller than $m_{irrigation\ water}$, so the above equation could be simplified as:

$$c_{soil\ extract} = \frac{m_{soil}\, c_{initial\ soil} + m_{irrigation\ water}\, c_{irrigation\ water}}{m_{irrigation\ water}} \#(5)$$

The soil extract was divided into two parts during soil remediation: soil flux, i.e., water evaporated from soil surface and water retained in the soil, and desalination flux, water evaporated from the desalter and water retained in the desalter.

Similarly, the salt in the soil extract was divided into two parts: the salt remaining in the soil and the salt entering the desalter. These two parts of salt were directly proportional to soil flux and desalter flux.

$$m_{salt\ in\ remediated\ soil} = \left(\frac{m_{soil}\, c_{initial\ soil}}{m_{irrigation\ water}} + c_{irrigation\ water}\right) m_{soil\ flux} \#(6)$$

$$m_{desalter} = \left(\frac{m_{soil}\, c_{initial\ soil}}{m_{irrigation\ water}} + c_{irrigation\ water}\right) m_{desalter\ flux} \#(7)$$

$$c_{remediated\ soil} = \left(\frac{c_{initial\ soil}}{m_{irrigation\ water}} + \frac{c_{irrigation\ water}}{m_{soil}}\right) m_{soil\ flux} \#(8)$$

Here, $m_{salt\ in\ remediated\ soil}$ was the mass of the salt in the remediated soil. $m_{soil\ flux}$ was the mass of soil flux. $m_{desalter}$ was the mass of desalter. $m_{desalter\ flux}$ was the mass of desalter flux. $c_{remediated\ soil}$ was the salinity of remediated soil.

The salinity of the remediated soil was directly proportional to the initial salinity, irrigation water salinity, and soil flux, and inversely proportional to the irrigation water mass. Therefore, the salinity of the remediated soil could be decreased by irrigating with lower salinity water, reducing soil flux, and increasing irrigation water mass. The specific methods included covering the soil with mulching film, wicking more water from the soil by desalter with stronger hygroscopicity, and changing soil structure to reduce soil water retention. However, the last option was not adopted because of its destructive effect on the soil.

Supplementary Note 4

Geometry model and description of the problem

A complex two-phase flow diffusion process exists in the phenomenon of salt confinement. The saltwater is continuously drawn up from the bottom by capillary action

through the filter paper, expelling the air originally trapped in the filter paper interstices. Meanwhile, there is a continuous convective diffusion process in the saltwater on the filter paper. Evaporation occurs constantly on the side of the filter paper containing saltwater, leading to an overall increase in saltwater concentration on the filter paper. At different stages, convection, diffusion, and evaporation have different effects. During the capillary absorption process of saltwater, the convection process often has a dominant function, and after the solution is no longer changing, the evaporation mechanism has a major influence. The diffusion process is mainly affected by the diffusion coefficient of the solute in the solution.

In this work, we used COMSOL Multiphysics software based on the finite element method to simulate a model of the "salt confinement." The geometry parameters are present in the Table S5. Table S6 lists the property parameters of the fluid and the working conditions in the model.

Supplementary Note 5

Governing equation

For the flow field, the mass conservation and the Navier-Stokes equations were used to solve the fluid dynamic characteristic:

$$\nabla \cdot U = 0 \#(9)$$

$$\rho\frac{\partial U}{\partial t} + \rho(U \cdot \nabla)U = \nabla \cdot \left[- pI + \mu\left(\nabla U + (\nabla U)^T\right)\right] \#(10)$$

For the two-phase flow, the phase field method is used to track moving interfaces by solving two transport equations. The phase field variable φ and the mixing energy density ψ are proposed to control the variable of the flow field:

$$\frac{\partial \phi}{\partial t} + U \cdot \nabla\phi = \nabla \cdot \frac{3\chi\sigma\varepsilon}{2\sqrt{2}}\nabla\psi \#(11)$$

$$\psi = \ - \nabla \cdot \varepsilon^2\nabla\phi + \left(\phi^2 - 1\right)\phi \#(12)$$

On the basis of the phase field method, we needed to modify the variable of the mass and momentum conservation equations as follows:

$$\rho = \rho_1 V_{f,1} + \rho_2 V_{f,2} \#(13)$$

$$\mu = \mu_1 V_{f,1} + \mu_2 V_{f,2} \#(14)$$

$$V_{f,1} = \frac{1 - \phi}{2}, V_{f,2} = \frac{1 + \phi}{2} \#(15)$$

For the diffusion process of salt accompanying the solution in the filter paper, because salt actually appears only in the part where the solution phase is located, a modified convection-diffusion equation can be expressed as follows:

$$\frac{\partial c}{\partial t} + V_{f,1}\nabla \cdot \left(- D_c\nabla c\right) + V_{f,1}u \cdot \nabla c = S \#(16)$$

Taking into account the effect of water evaporation in the solution, we included the increase in salt concentration after evaporation in the source term. Therefore, the expression for calculating the source term can be inferred as follows:

$$S = \frac{4Fc}{\rho D\eta} \#(17)$$

Supplementary Note 6

Boundary condition

At the bottom of the model, the velocity and concentration inlet condition were set as follows:

$$c = c_0 \#(18)$$

$$U = u(t)n \#(19)$$

At the top of the model, only air comes out. The outflow condition without diffusion was set as follows:

$$p = p_0 \#(20)$$

At the side wall of the model, the wall boundary condition is defined as the absence of fluid outflow and material diffusion. according to the numerical simulation. The change of the salt mass fraction is caused by the evaporation of the water. The real influence is considered in the source term in the Eq. (16-17). So the wall condition was set as follows:

$$n \cdot U = 0 \#(21)$$

$$-n \cdot \left(-D_c \nabla c\right) = 0 \#(22)$$

Supplementary Note 7

The construction checklist for the brine desalter model with a daily output of one ton of freshwater, which could operate for 20 years, was divided into a construction section (Table S3) and a maintenance section (Table S4). The construction section referred to the freshwater storage tank, condensing shell, bracket, pipe, collector, pump, sealant, and electricity for the pump during the construction and operation process. These items would not change by default during the 20-year operation. The maintenance section referred to the paper, polylactic acid, tape, and electricity consumed in the production of the desalter. These items needed to be replaced during the 20-year operation because of the expiration of the desalter's service life, and the consumption for only one replacement is listed here.

Area of desalination device: The desalination device was constructed based on the desalter array described in Figure S14. The desalination device would operate at a 100% evaporation

rate for 8 h during the day and at a 40% evaporation rate for 16 h at night. The area of the desalination device was calculated according to the following formula:

$$S = 1000 \div (m_{mass\ change} + m_{mass\ change} \times 0.4 \div 8 \times 16) \#(23)$$

S is the area of the desalination device, and $m_{mass\ change}$ is the mass change per unit area of the desalter array during the day.

Maintenance section:

Tank: The desalination device was equipped with a freshwater storage tank (capacity: 1 t). The tank was a cube (length: 1 m, wall thickness: 0.25 cm, material: polyvinyl chloride, PVC). The density of all PVC was calculated based on 1340 kg m^{-3}. The mass of the storage tank was calculated according to the following formula:

$$m_{tank} = 1 \times 1 \times 6 \times 0.0025 \times 1340 \#(24)$$

m_{tank} is the mass of the tank.

Condensing shell: The condensing shell (cuboid, height: 0.25 m, wall thickness: 0.25 cm) was composed of PVC materials. It was spliced by PVC sheets with a side length of 1 m, which was a common PVC sheet size on the market. The mass of the condensing shell was calculated according to the following equation:

$$m_{condensing\ shell} = (2 \times S + \sqrt[2]{S} \times 0.25 \times 4) \times 0.0025 \times 1340 \#(25)$$

$m_{condensing\ shell}$ is the mass of the condensing shell.

Bracket: Because the condensation shell was spliced by PVC sheets, brackets were necessary to support the sheets. Horizontal brackets were installed at the juncture of every two boards, and longitudinal brackets were installed at the intersection of these horizontal brackets. The bracket material was PVC. The mass of the bracket was calculated according to the following formula:

$$m_{bracket} = (10 \times \sqrt[2]{S} + 0.25 \times 49) \times 0.02 \times 0.02 \times 1340 \#(26)$$

$m_{bracket}$ is the mass of the bracket.

Pipe and collector: An L-shaped collector composed of eight PVC pieces with a width of 3 cm was installed around the condenser to collect the condensate water, and a water pipe (1.5 kg weight) was equipped for water inlet and outlet. The mass of the pipe and condenser was calculated according to the following formula:

$$m_{tube} = \sqrt[2]{S} \times 8 \times 0.03 \times 0.0025 \times 1340 + 1.5 \#(27)$$

m_{tube} is the mass of the pipe and collector.

Pump: A water pump (14 kg, cast iron) with a power of 1.1 kW and a flow rate of 3 m^3 h^{-1} was used to supply water to the desalination device.

Sealant: Sealant (0.8 kg) was used to seal the gaps between PVC sheets. It was replaced by PDMS for the calculation of LCA.

Insulation sponge: The bottom and sides of the condensation shell were wrapped with polyurethane sponges (PU, thickness: 3 cm) to prevent heat loss. The sponge density was 40 kg m^{-3}. The mass of the polyurethane sponge was calculated according to the following formula.

$$m_{PU} = (S + \sqrt[2]{S} \times 0.25 \times 4) \times 0.03 \times 40\#(28)$$

m_{PU} is the mass of the PU sponge.

Electricity: Used to drive the pump to supply water to the desalination device. The water supply was 1 t per day for 20 years. The electricity consumption for water supply was calculated according to the following formula:

$$W_{pump} = 1 \div 3 \times 1.1 \times 365 \times 20\#(29)$$

W_{pump} is the electricity consumed by the pump.

Maintenance section

Number of desalters: The installation density was 2500 desalters per square meter. The number of desalters for one replacement was calculated according to the following formula:

$$N = S \times 2500\#(30)$$

N is the number of desalters.

Paper: Each desalter was wrapped with 74.8 cm^2 of paper with a density of 80 g m^{-2}. The paper was replaced by cellulose fiber for the calculation of LCA. The mass of paper for one replacement was calculated according to the following formula:

$$m_{paper} = N \times 0.00748 \times 80 \div 1000\#(31)$$

m_{paper} is the mass of paper.

Polylactic acid: Each desalination unit contained one 1.11g PLA straw. The mass of PLA required for one replacement was calculated according to the following formula:

$$m_{PLA} = N \times 1.11 \div 1000\#(32)$$

m_{PLA} is the mass of PLA.

Tape: Used to bond paper to the surface of straws; each desalter required 68.2 mg of tape. The tape was replaced by 50% polyethylene terephthalate and 50% acrylic acid for the calculation of LCA. The mass of tape required for one replacement was calculated according to the following formula:

$$m_{tape} = N \times 68.2 \div 1000000\#(33)$$

m_{tape} is the mass of tape.

Mulching film: PE film with a thickness of 10 um was selected as mulching film. The density of PE was 940 kg m^{-3}. The mass of the mulching film was calculated according to the following formula:

$$m_{mulching\ film} = S \times 10 \times 10 - 6 \times 940\#(34)$$

$m_{mulching\ film}$ is the mass of mulching film.

Electricity: Equipment with a power of 2 kW and a production speed of 300 units per minute was used to produce the desalter. The electricity consumption for one replacement was calculated according to the following formula:

$$W_{desalter} = N \div 300 \div 60 \times 2\#(35)$$

$W_{desalter}$ the electricity consumed by desalter production.

Supplementary Note 8

The global water resource distribution data were provided by the World Resources Institute. The global saline-alkali land distribution data were provided by the United Nations Food and Agriculture Organization. Global wheat production data were provided by EarthStat.

The impact of saline-alkali land remediation with the paper-based columnar desalter on global wheat production was predicted based on the research of Lamsal et al. The relation between wheat yield and soil salinization was shown as follows:

$$Y = 1.009 - 0.02EC\#(36)$$

Y is the relative yield of wheat, and EC is the soil conductivity (mmhos cm^{-1}, equal to mS cm^{-1}).

The global saline-alkali land distribution data provided by FAO did not specify the testing method for the soil conductivity data. Therefore, we assumed that soil conductivity was measured by a soil extraction method with a water-to-soil ratio of 5:1; this method is a common soil conductivity assay.

Supplementary Figures

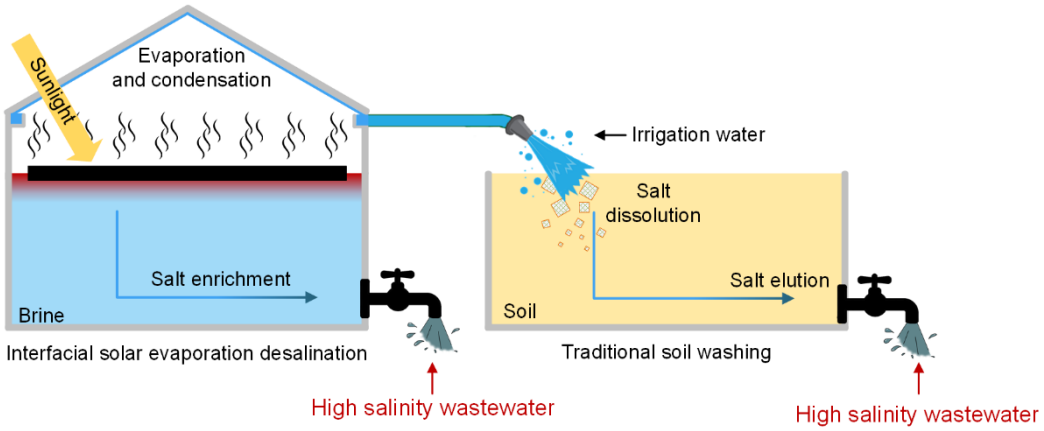

Figure S1. The traditional remediation method that interfacial solar evaporation produces freshwater and then the freshwater is used for soil washing, in which both interfacial solar evaporation and soil washing generate a large amount of high-salinity wastewater.

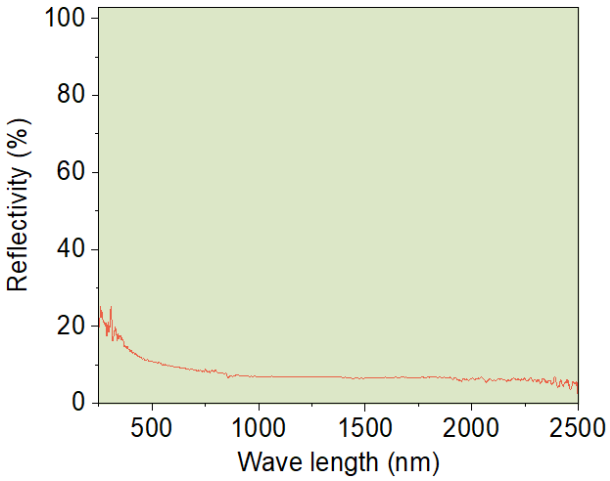

Figure S2. The reflection spectrum of mulching film, showing extremely low reflectivity.

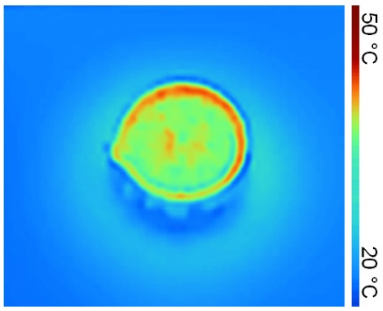

Figure S3. The mulching film heated to 42 °C by sunlight, appearing warm color in infrared image due to a large amount of infrared light emitted by it.

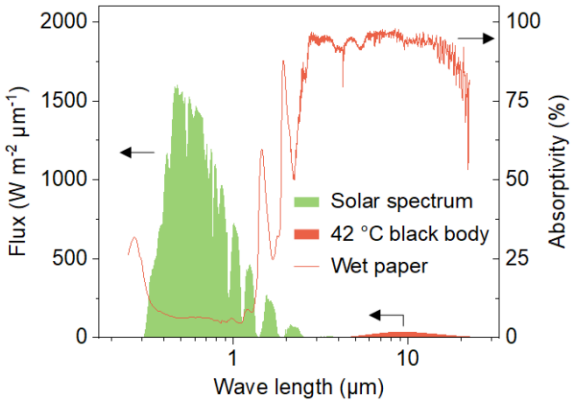

Figure S4. The absorption spectrum of the wet paper, the solar spectrum and the blackbody radiation spectrum at 42 °C that is isothermal with the mulching film, indicating the infrared radiation emitted by the mulching film can be efficiently absorbed by the wet paper.

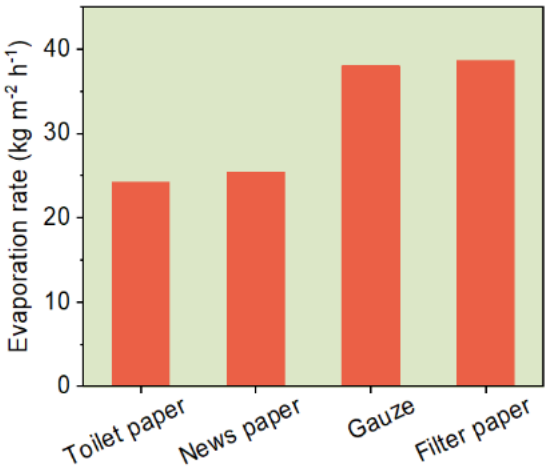

Figure S5. The evaporation rate of desalination devices made of different materials. Although various materials could be used for constructing desalters, the filter paper-based desalter had the highest evaporation rate.

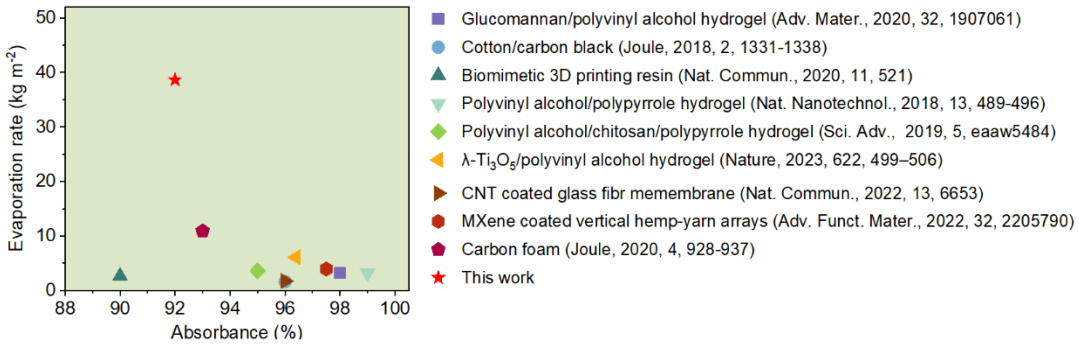

Figure S6. Evaporation rates of paper-based columnar desalter and other reported evaporators, indicating that the paper-based columnar desalter had the highest evaporation rate.

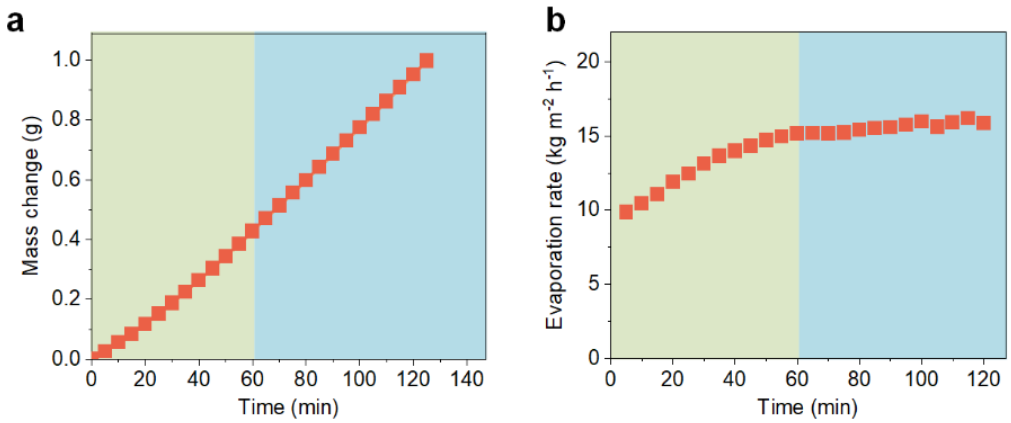

Figure S7. The time-dependent (a) mass change and (b) evaporation rate of the columnar desalter under dark conditions, indicating that the desalination devices stably operated in the dark.

Chloride ion rapid test strip

Figure S8. The test results of chloride ion detection test paper for the concentration of brine in the beaker. There was no difference in the color of the chloride ion detection test paper before and after being stored in the dark for 12 h, indicating that the salt entering the desalters had hardly returned to the bottom bulk water.

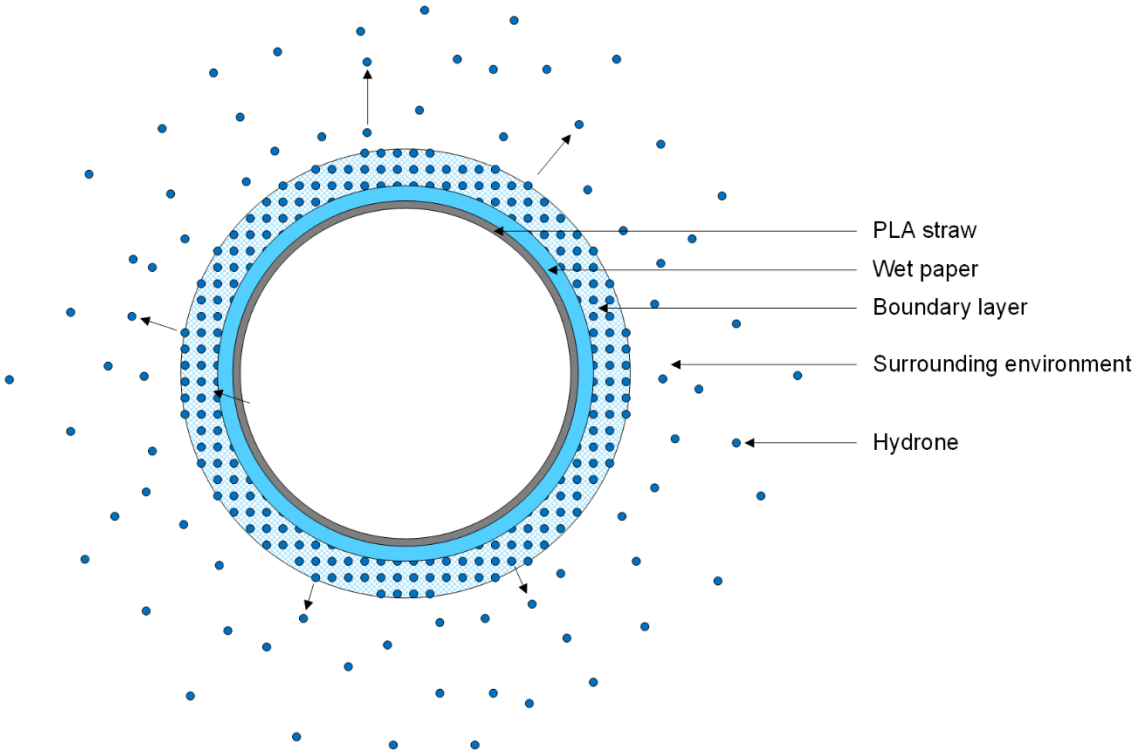

Figure S9. The schematic diagram of water evaporation in the desalter, showing the migration path of water molecules from the wet paper to the boundary layer and then to the surrounding environment.

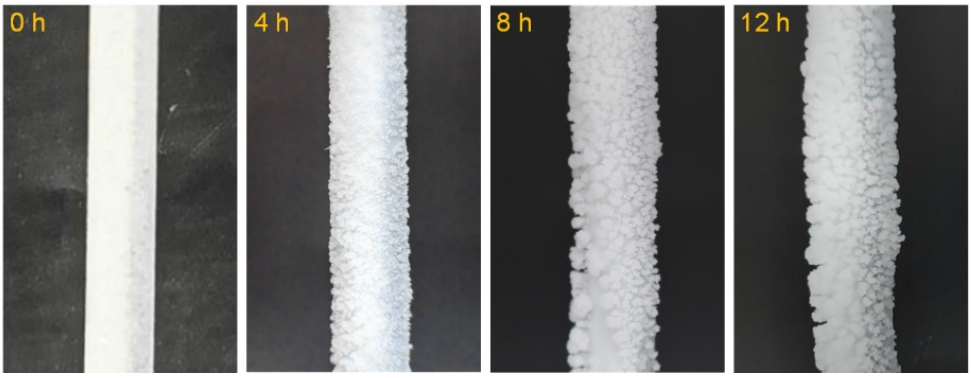

Figure S10. The process of salt accumulation on the surface of the desalter, which made the surface of the desalter rough.

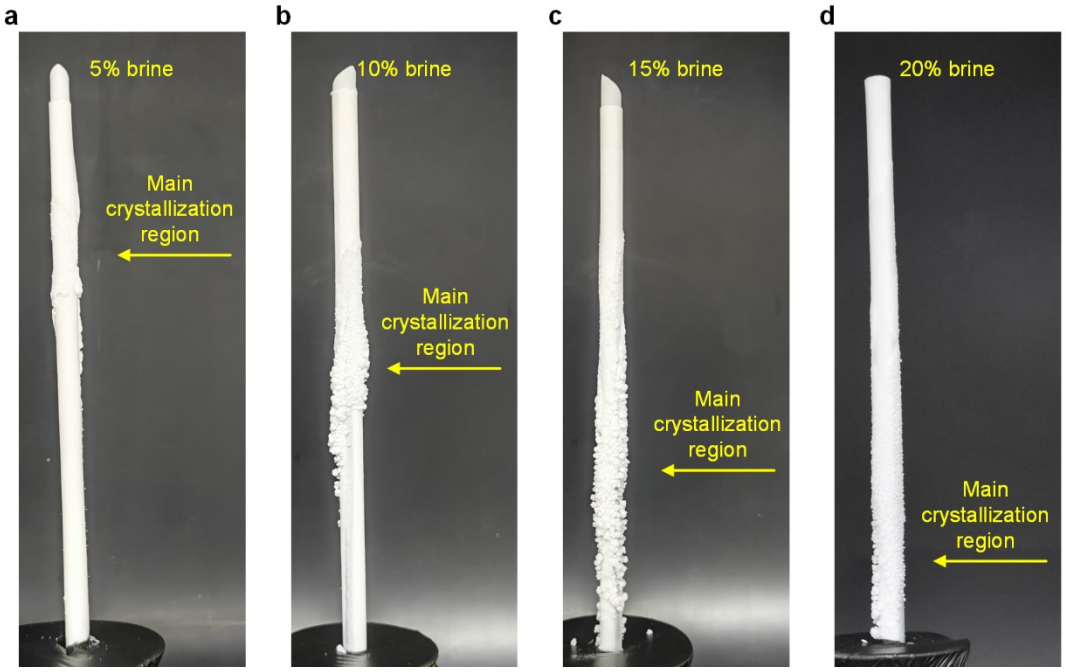

Figure S11. The crystallization sites of salt on the surface of desalter in brine with salinities of (a) 5%, (b) 10%, (c) 15% and (d) 20%, showing the positional selectivity of crystallization.

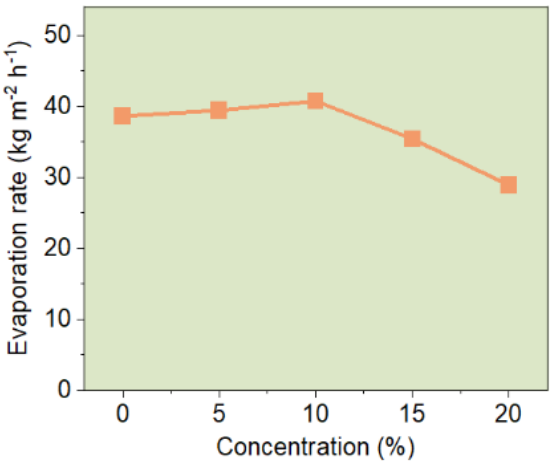

Figure S12. The evaporation rate of desalter in different concentrations of brine, exhibiting the salt-resistance of the desalters in the low salinity brine.

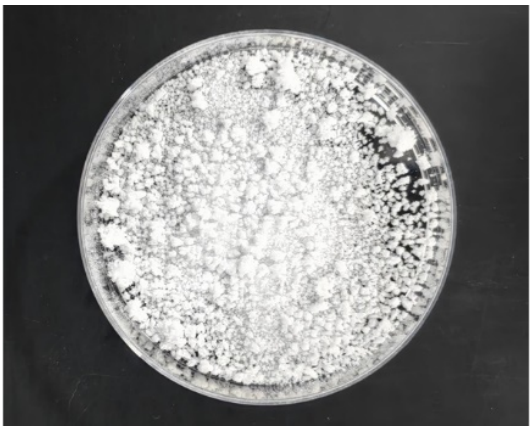

Figure S13. The salt collected from the surface of the desalter, indicating the ability to recover salt resources from brine.

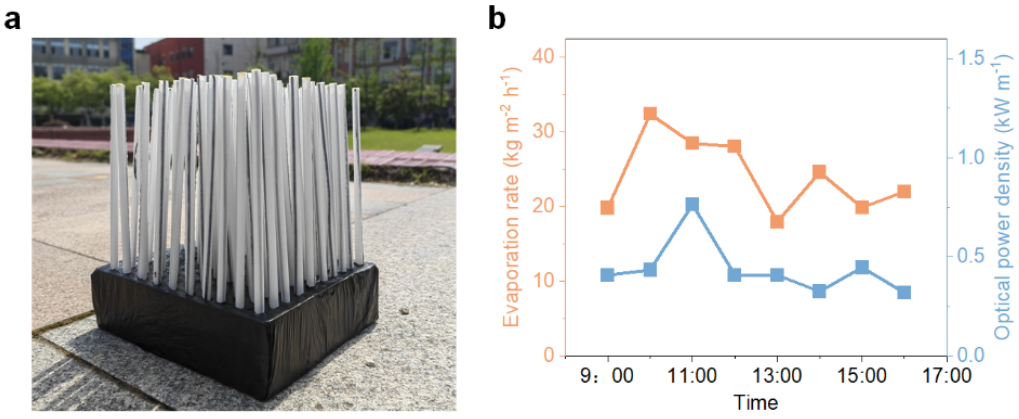

Figure S14. (a) The 10×10 desalter array and (b) its evaporation rate under natural light, showing the enormous potential for stable operation under natural light.

Figure S15. (a) A desalter array with a condensing shell, and (b, c) the condensed water on its surface, confirming its enormous potential in freshwater production.

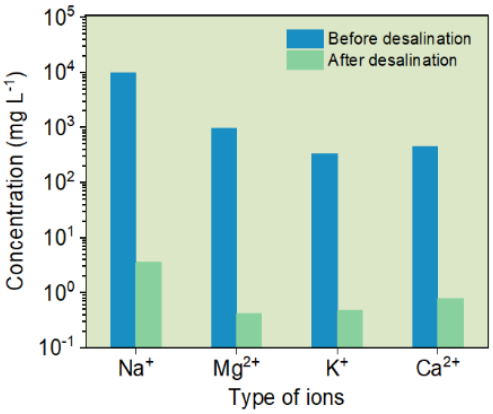

Figure S16. The concentration of major ions in the Huanghai Sea seawater before and after desalination, demonstrating the extremely high ion removal efficiency of 99.9%.

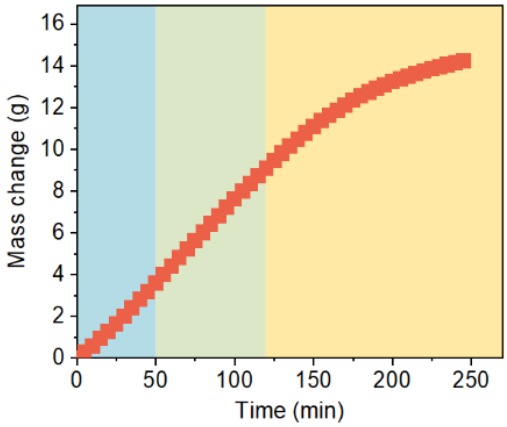

Figure S17. The mass change of soil desalination device with time during soil remediation (blue: rising period; green: plateau; yellow: decrements, only suitable for Figure S17).

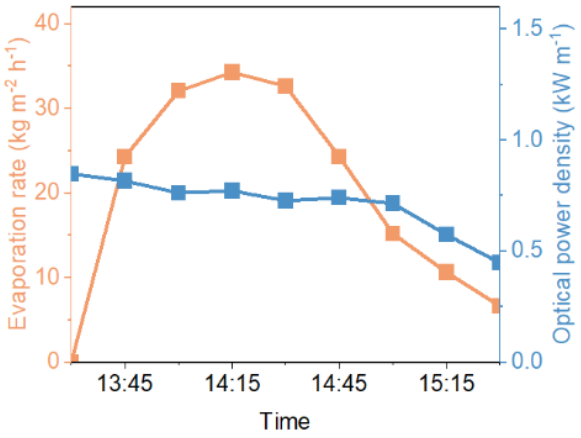

Figure S18. The evaporation rate of soil desalination devices under natural light, exhibiting an evaporation rate greater than that under simulated sunlight and showing enormous potential for practical applications.

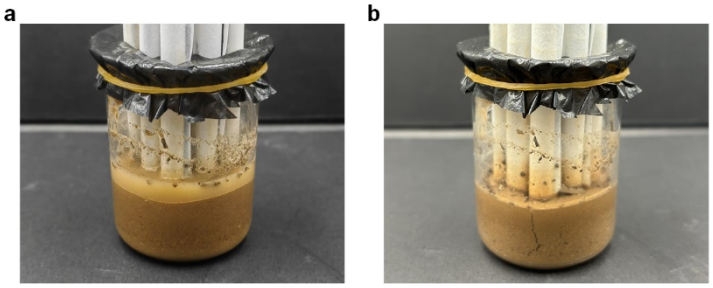

Figure S19. Irrigation water accumulated in the soil (a) before and (b) after soil remediation, showing the fluxible water was completely evaporated and demonstrating the zero-liquid discharge of the soil remediation process.

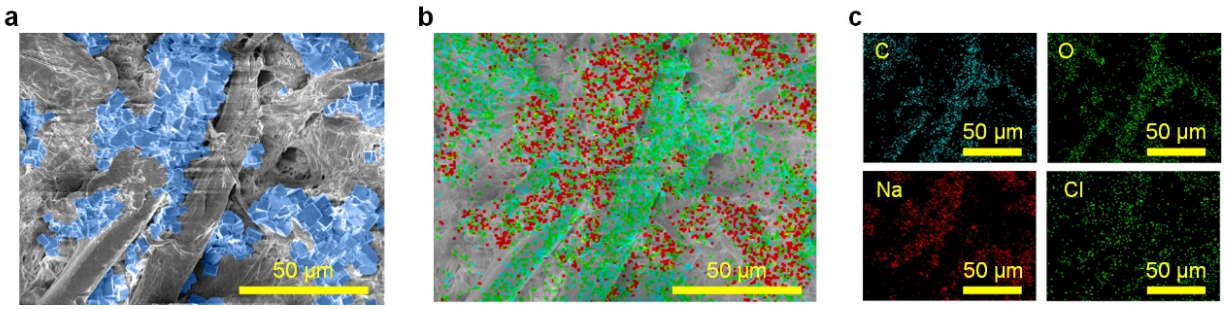

Figure S20. (a) SEM and (b and c) EDS images of the surface of the desalter after saline-alkali soil remediation, showing the confined salt in the desalters.

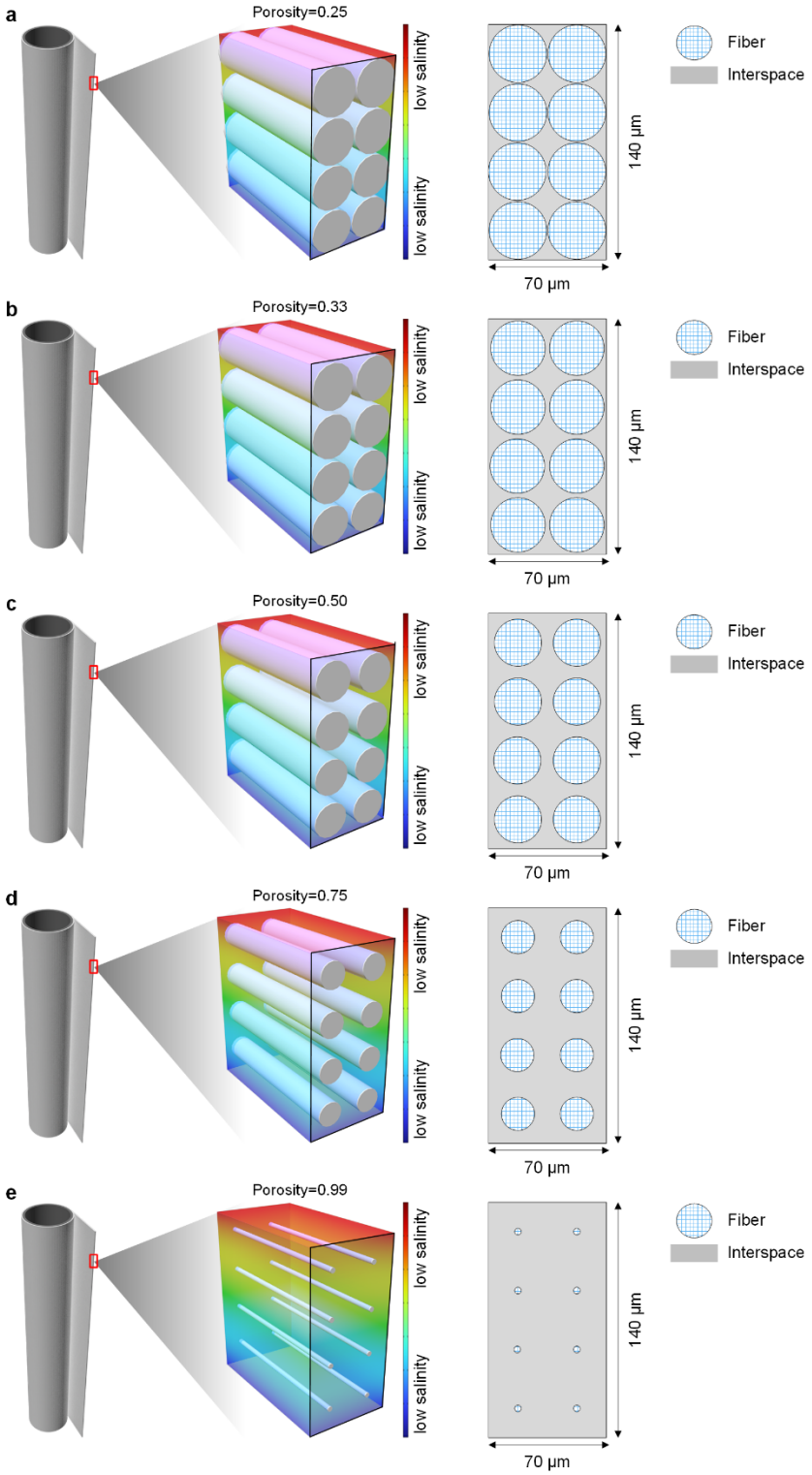

Figure S21. Flow channel models for computational fluid dynamics of paper with different porosity, (a) porosity of 0.25, (b) porosity of 0.33, (c) porosity of 0.50, (d) porosity of 0.75, and (e) porosity of 0.99.

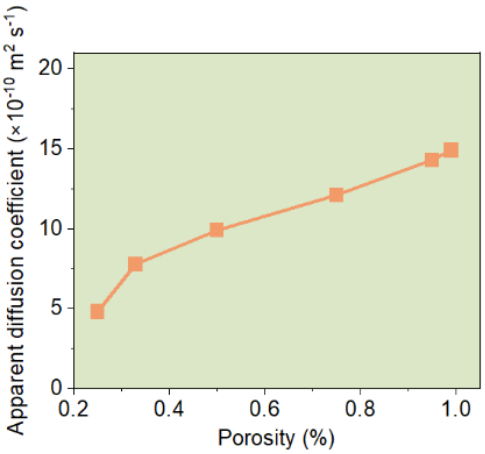

Figure S22. The apparent diffusion coefficient of filter paper models with different porosity, indicating the apparent diffusion coefficient and porosity were directly proportional.

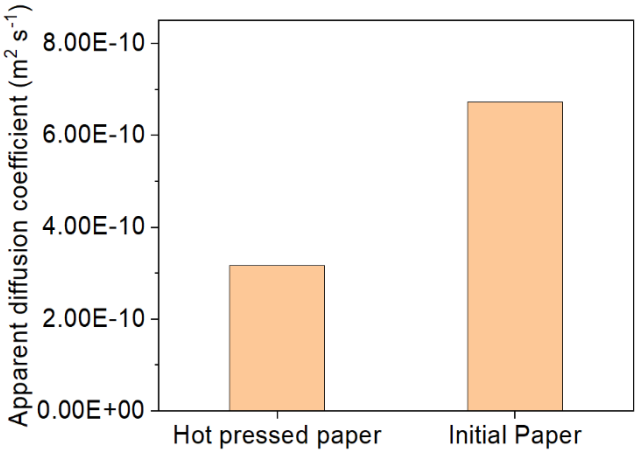

Figure S23. Apparent diffusion coefficients of hot pressed paper (porosity 50.6%) and initial paper (porosity 67.3%).

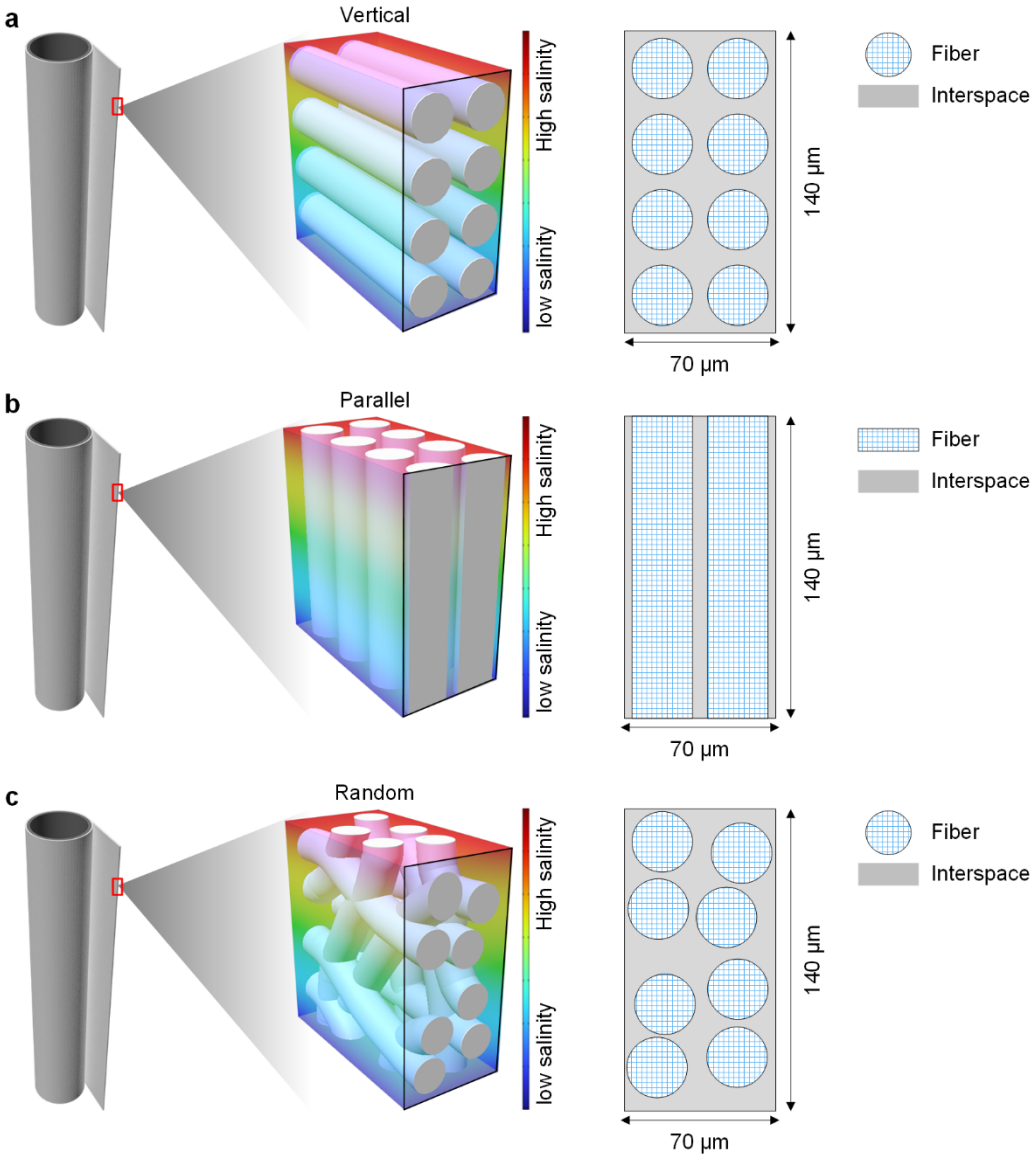

Figure S24. Flow channel models for computational fluid dynamics of paper with different fiber arrangements, (a) vertical, (b) parallel, and (c) random.

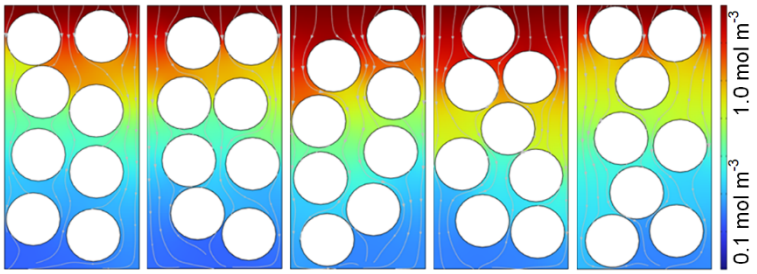

Figure S25. The filter paper models with different fiber arrangement modes, verifying that random fiber arrangement reduced the apparent salt diffusion coefficient.

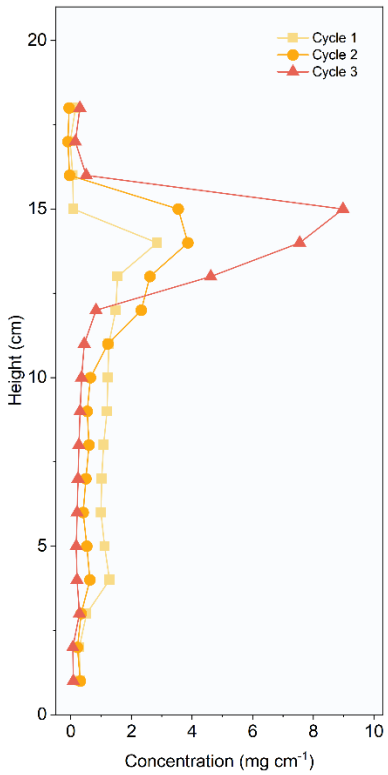

Figure S26. Salt distribution in desalters during soil remediation.

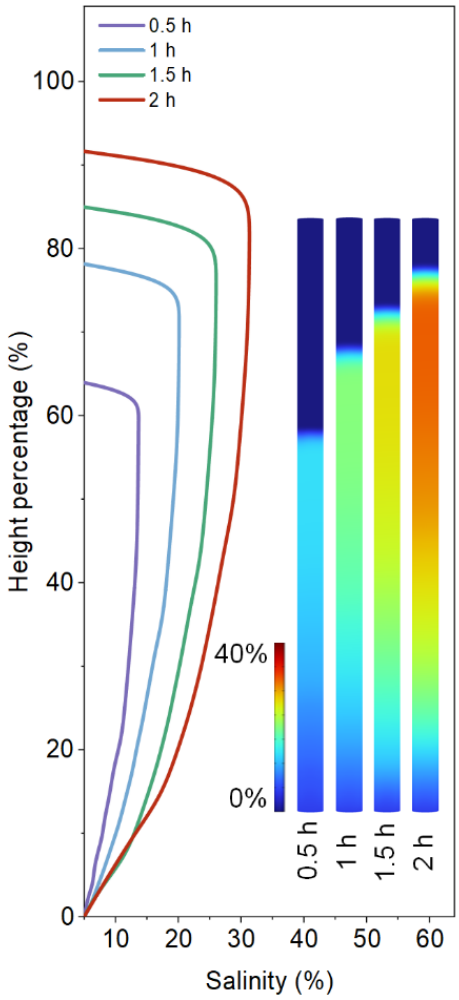

Figure S27. The variation of salt concentration distribution in desalter models during brine desalination. The concentration at the bottom inlet remained low, indicating that almost no salt escaped from the inlet to the bottom bulk water during brine desalination. Blue represents low salinity, red represents high salinity.

Figure S28. The paper-based desalter produced rapidly and wholesale by the mature straw packaging production line from the beverage and package industries, confirming the feasibility of large-scale production of desalter.

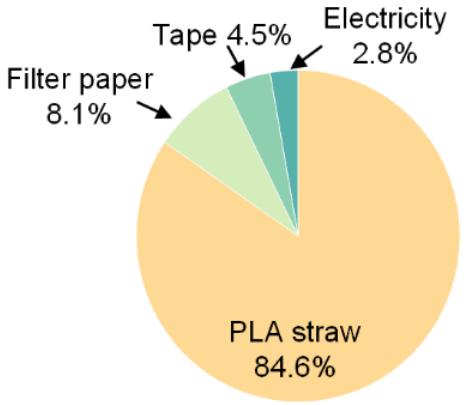

Figure S29. The composition of CO_2 emission during the desalter production, indicating that PLA was the main source of CO_2.

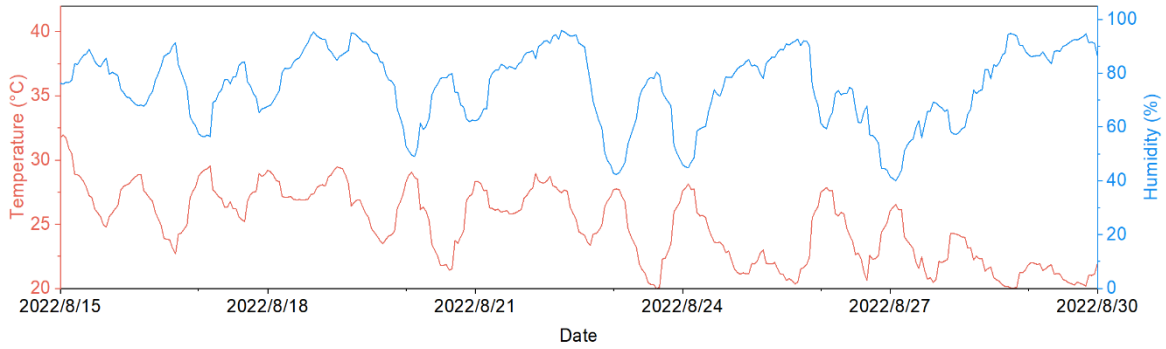

Figure S30. Changes in temperature and humidity during the field experiment.

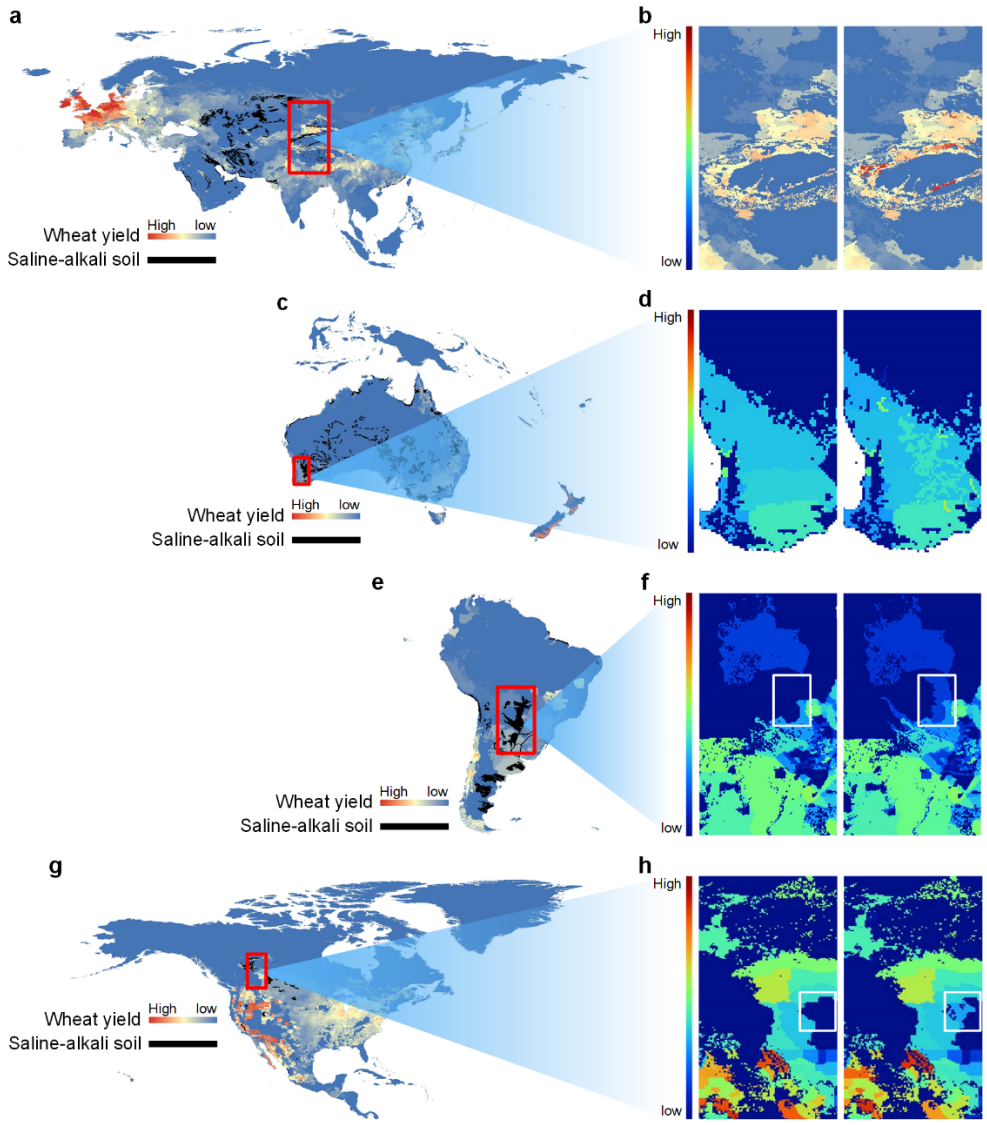

Figure S31. Global wheat production and distribution of saline-alkali land and wheat yield before and after remediation. (a) The wheat production and distribution of saline-alkali land in Asia and Europe, (b) wheat production in parts of northwest China and surrounding areas, (c) wheat production and distribution of saline-alkali land in Oceania, (d) wheat production in Perth and surrounding areas, (e) wheat production and distribution of saline-alkali land in South America, (f) wheat production in Paraguay and surrounding areas, (g) wheat production and distribution of saline-alkali land in North America, (h) wheat production in Alberta of Canada, Montana of United States and surrounding areas.

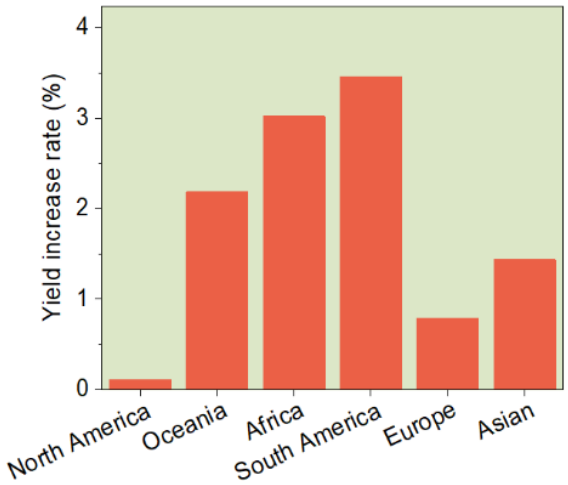

Figure S32. Wheat yield forecast on six continents, indicating that the desalter has an important function in increasing wheat yield in South America, Africa and Oceania.

Supplementary Tables

Table S1 The amount of salt returning from desalter to bulk water.

Salinity of bulk water (%)	5	10	15	20
Salt returning (%)	2.71	0.74	1.63	0.87

Table S2 Cost accounting of the paper-based columnar desalter.

Item	Filter paper	PLA	Tape	Electricity	Total
Cost of per million desalters ($)	1412.31	3772.45	2174.55	10.11	7369.41

Table S3 Construction list.

Item	Consumption
tank	20.10 kg
condensing shell	248.65 kg
bracket	37.92 kg
pipe and collector	6.20 kg
pump	14 kg
sealant	0.8 kg
insulation sponge	48.04 kg
electricity	2676.67 kW h

Table S4 Maintenance list.

Item	Consumption
paper	51.15 kg
PLA	94.87 kg
tape	5.83 kg
mulching film	0.32 kg
electricity	9.49 kW h

Table S5 Geometrical parameters of the model

Geometrical parameters	**Value**
Inner diameter of filter paper D_{in} (mm)	5.92
Outer diameter of filter paper D_{out} (mm)	6.56
Length of the filter paper L_1 (mm)	150
Volume ratio of filter paper η	0.682

Table S6 The property parameter of the computational domain

Property parameters	**Value**
The density of the air ρ_a (kg/m^3)	1.2
The density of the salt ρ_s (kg/m^3)	2000
The density of the water ρ_w (kg/m^3)	997
Dynamic viscosity coefficient of the salt water μ_w (Pa·s)	1e-3
Dynamic viscosity coefficient of the air μ_a (Pa·s)	1.1e-5
Diffusion coefficient of the salt D_c (m^2/s)	1.5e-9